(Preprint) AAS 25-168

GOAL-ORIENTED GUIDANCE UNDER UNCERTAINTIES FOR SMALL BODIES PROXIMITY OPERATIONS

Antonio Rizza*, Simone D'Amico† and Francesco Topputo‡

Proximity operations to minor bodies demands high levels of autonomy to achieve cost-effective, safe and reliable solutions. Autonomous trajectory planning plays a pivotal role, requiring intelligent targeting of mission objectives. A goal-oriented guidance strategy robust to navigation and control uncertainties and based on the combination of abstract reachability analysis and sequential convex programming is presented in this paper. The methodology is embedded in a model predictive control framework allowing for fast replanning and compensation of unmodelled dynamics. Eros proximity operations are considered to validate the approach successfully targeting mission objectives.

1 INTRODUCTION

In the last twenty years, the space sector has experienced an unprecedented growth, marked by significant advancements and achievements both concerning Earth's orbiting and deep-space missions. The recent growing interest in small solar system bodies such as asteroids and comets for scientific inspection, exploitation of resources, and planetary defense reasons is pushing the development of innovative engineering solutions to better investigate these celestial bodies. Ground-based observations allow preliminary characterizations of small bodies in terms of bulk properties such as orbit, mass, shape, rotational state, and surface composition. The major limitation of this methodology is the signal to noise ratio which is acceptable only when the target is relatively close to the Earth.[1] A drastic improvement in the body characterization can be obtained with in-situ observations with the use of specialized and instrumented probes. Several missions successfully performed proximity operations to these bodies such as the Near Earth Asteroid Rendezvous (NEAR) Shoemaker,[2] Dawn,[3] the Origins, Spectral Interpretation, Resource Identification, Security, Regolith Explorer (OSIRIS-REx),[4] Hayabusa,[5] Hayabusa 2,[6] Rosetta,[7] and the Double Asteroid Redirection Test (DART).[8,9]

All these missions share a similar concept of operations. They are, in fact, all characterized by three key elements: 1) a heavy workload on the ground segment to operate the probe, 2) the need for an extended far-range remote sensing to characterize target and environment before being able to perform close proximity operations, and 3) a marginalized propellant strategy to cope with uncertainties and potential mission extensions. This comes in contrast with the current transition to

*PhD Candidate, Department of Aerospace Science and Technology (DAER), Politencico di Milano, Via La Masa 34, antonio.rizza@polimi.it.

†Associate Professor, Department of Aeronautics and Astronautics, Durand Building, 496 Lomita Mall, damicos@stanford.edu

‡Full Professor, Department of Aerospace Science and Technology (DAER), Politencico di Milano, Via La Masa 34, francesco.topputo@polimi.it.

miniaturized platforms for systematic deep-space exploration,[10] in which low budget missions are being developed willing to accept larger risks in sight of a bigger reward.

Current approaches for autonomous proximity operations often rely on tracking a reference trajectory previously designed on-ground. This approach allows for no replanning capability, struggling in facing unforeseen events. Moreover, the design is often targeting the best solution in terms of fuel consumption or time of flight, imposing weak requirements in terms of trajectory envelope that do not generally consider the body rotation and shape. The satisfaction of observation and mapping requirements, typically relies on the fact that the target rotational period is significantly shorter than the orbital one, leading to an higher probability of achieving global mapping. However, this framework breaks down for different reasons when more complex objectives are considered such as the observation of a specific set of surface features at a given resolution or under specific illumination conditions. When the perturbing effect of solar radiation pressure and distributed gravity is considered, the very existence of stable closed orbits is compromised often leading to high station keeping costs. At the same time, replanning capability and target mapping requires accurate knowledge on the system dynamics, and precise estimation of the spacecraft state, which are strongly affected by dynamics, navigation and control uncertainties. Finally, the minimization of fuel consumption, may not be of primary importance when performing small bodies proximity operations because of the high connectivity of the configuration space that allows for relatively fast and cheap reconfiguration.

An innovative concept developed in recent years is proposing a paradigm shift towards autonomous goal-oriented approaches.[11] The idea is that the probe is provided with the high-level objectives of the mission and the trajectory is computed autonomously on-board within a continuous replanning framework to best achieve the assigned tasks. In literature this problem is solved, under the assumption of impulsive control, by means of abstract reachability analysis performed in the control domain framed within a receding horizon model predictive control framework.[12,13] The authors also extended this approach to multiple bodies observations and more challenging tasks.[14,15] While being very flexible to different mission scenarios and observation requirements, this approach alone presents a few limitations mainly due to the computational cost of the reachable sets. An alternative methodology is proposed in Rizza et al.[16] to perform goal-oriented path planning within a Sequential Convex Programming (SCP) framework. SCP is a direct optimization method used to solve non-convex optimization problem via sequential convexification that approximate the cost function and the constraints of the original problem in the neighbourhood of the previous step solution.[17,18] However, like all direct methods, the efficiency of this strategy heavily depends on the quality of the initial guess solution. This paper introduces a mixed approach that combines the flexibility of reachability with the efficiency of SCP to achieve autonomous goal-oriented guidance under uncertainties.

In particular, a methodology based on three functional blocks is proposed here, as shown in Figure 1. The first element consists in translating high-level scientific requirement into a set of operative requirements; then by taking into account operational and safety constraints a pipeline to rapidly generating a reference trajectory is proposed. The obtained guidance profile is refined in the third block of the figure taking into account for navigation and control uncertainties. The full pipeline is then embedded within a Model Predictive Control (MPC) framework to compensate for dynamics uncertainties.

Two main contributions are provided to the state of the art in this work: 1) a gradient based abstract reachability analysis scheme is introduced for fast generation of deterministic trajectories,

and 2) a joint reachability-SCP scheme is proposed to refine the deterministic trajectory within an uncertainty robust framework.

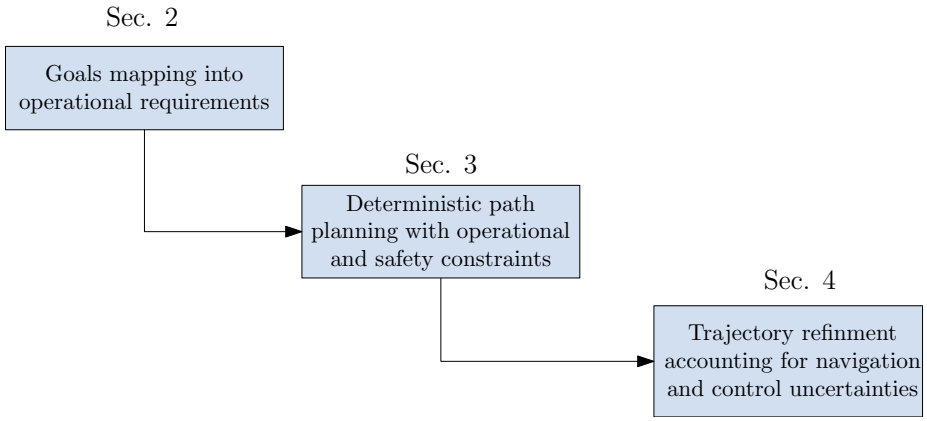

Figure 1: Main building blocks of the proposed methodology.

The structure of the paper is the following, Section 2 presents the process used to map high-level scientific goals to operational constraints, Section 3 illustrates the gradient-based reachability scheme used to generate the deterministic control profile and Section 4 shows the SCP scheme used to refine the trajectory under uncertainties. The three elements are merged together in Section 5 within an MPC framework and Section 6 proposes the application of the proposed approach to the case of asteroid (433) Eros proximity operations. Major findings and conclusions are finally discussed in Section 7. The adopted nomenclatuere and conventions used across this paper is detailed in the Appendix.

2 ABSTRACT GOALS REPRESENTATION

Mission objectives, also referred to as goals in the framework of this work, are generally high level concepts often specified in a qualitative way. To guide the space mission engineering process, these conditions are expanded in a series of quantitative and verifiable statements known as requirements. Combining science requirements with the on-board payload specifications, mission goals are converted in measurements and operational requirements. This work is developed under the assumption that the high-level objective of the mission is the characterization of a finite number of features on the asteroid surface within a given range $\rho_i \in [\rho_i^-, \rho_i^+]$, emission angle (between the spacecraft and the surface normal) $\theta_i \in [0, \theta_i^+]$, and inclination angle (between the Sun and the surface normal) $\beta_i \in [0, \beta_i^+]$ as shown in Figure 2. The first two are converted into the operational requirement of flying within a spherical sector Ω_i^P, above the asteroid's surface, while the third one constraints the time of the observation.

The three quantities are defined as

$$\begin{aligned}
\rho_i\left(\mathbf{x}\right) &= \sqrt{\left(\mathbf{r}_{\mathcal{B}}(\mathbf{x}) - \mathbf{r}_{i\mathcal{B}}\right)^T \left(\mathbf{r}_{\mathcal{B}}(\mathbf{x}) - \mathbf{r}_{i\mathcal{B}}\right)} \\
\theta_i\left(\mathbf{x}\right) &= \arccos\left(\frac{\mathbf{n}_{i\mathcal{B}}^T \left(\mathbf{r}_{\mathcal{B}}(\mathbf{x}) - \mathbf{r}_{i\mathcal{B}}\right)}{||\mathbf{r}_{\mathcal{B}}(\mathbf{x}) - \mathbf{r}_{i\mathcal{B}}||}\right) \\
\beta_i\left(\mathbf{x}, t\right) &= \arccos\left(\frac{\mathbf{n}_{i\mathcal{B}}^T \left(\mathbf{r}_{s\mathcal{B}}(t) - \mathbf{r}_{i\mathcal{B}}\right)}{||\left(\mathbf{r}_{s\mathcal{B}}(t) - \mathbf{r}_{i\mathcal{B}}\right)||}\right)
\end{aligned} \tag{1}$$

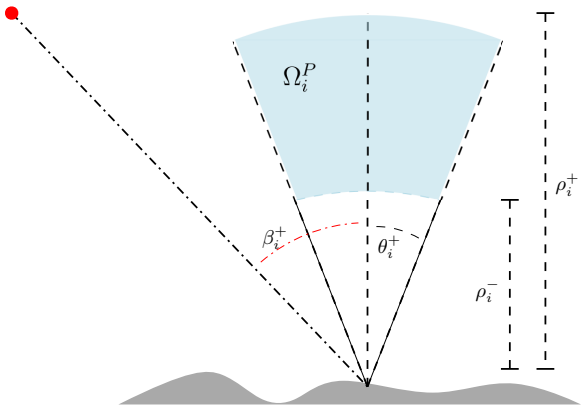

Figure 2: Geometrical interpretation of the observation region Ω_i^P and the quantities defining the operational constraints. The red dot indicates the Sun position.

where $\mathbf{r}_{\mathcal{B}}(\mathbf{x})$, $\mathbf{r}_{i\mathcal{B}}$ and $\mathbf{r}_{s\mathcal{B}}(t)$ refer respectively to the spacecraft, the feature, and the Sun position in the asteroid fixed frame $\mathcal{B}$, and $\mathbf{n}_{i\mathcal{B}}$ is the normal to the surface at the feature's location. An abstract mapping $\mathbf{y}_i = \mathbf{m}_i(\mathbf{x}, t)$ is then introduced to simplify the operational requirements representation with

$$\mathbf{y}_i = \begin{bmatrix} y_{i,1} & y_{i,2} & y_{i,3} \end{bmatrix}^T = \left[\left(\frac{\rho_i}{\overline{R}} \right)^2 \quad \cos(\theta_i) \quad \cos(\beta_i) \right]^T \tag{2}$$

with $\overline{R}$ being a reference length used to make the formulation of the map fully non-dimensional. In this abstract space, the operational requirements become the ones of flying through the polyhedral region Ω_i shown in Figure 3, called *observation region*.

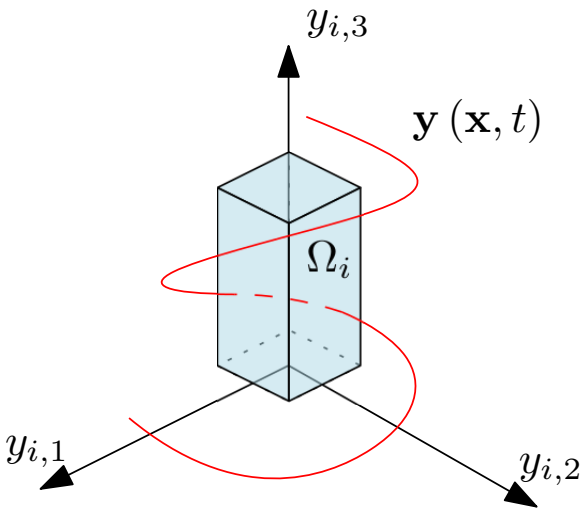

Figure 3: Spacecraft motion $\mathbf{y}(\mathbf{x}, t)$ and observation region Ω_i in the abstract space.

By adopting an inertial Cartesian state representation of the spacecraft state, i.e. $\mathbf{x} = \left[\mathbf{r}^T, \mathbf{v}^T\right]^T$,

the motion in the abstract space becomes

$$\begin{aligned} y_{i,1}(\mathbf{x},t) &= \frac{\mathbf{x}^T\mathbf{L}_{rr}\mathbf{x} + \mathbf{q}_i^T(t)\,\mathbf{x} + \mathbf{r}_{i\mathcal{B}}^T\mathbf{r}_{i\mathcal{B}}}{\overline{R}^2} \\ y_{i,2}(\mathbf{x},t) &= \frac{\mathbf{n}_{i\mathcal{B}}^T\left(\mathbf{R}_{\mathcal{N}2\mathcal{B}}(t)\,\mathbf{L}_r\mathbf{x} - \mathbf{r}_{i\mathcal{B}}\right)}{||\mathbf{R}_{\mathcal{N}2\mathcal{B}}(t)\,\mathbf{L}_r\mathbf{x} - \mathbf{r}_{i\mathcal{B}}||} \\ y_{i,3}(t) &= \frac{\mathbf{n}_{i\mathcal{B}}^T\left(\mathbf{r}_{s\mathcal{B}}(t) - \mathbf{r}_{i\mathcal{B}}\right)}{||\left(\mathbf{r}_{s\mathcal{B}}(t) - \mathbf{r}_{i\mathcal{B}}\right)||} \end{aligned} \tag{3}$$

with $\mathbf{R}_{\mathcal{N}2\mathcal{B}}$ being the rotation matrix from the inertial frame $\mathcal{N}$ to the asteroid fixed frame $\mathcal{B}$ and $\mathbf{q}_i(t) = -2\mathbf{L}_r^T\mathbf{R}_{\mathcal{N}2\mathcal{B}}^T(t)\,\mathbf{r}_{i\mathcal{B}}$.

3 GRADIENT-BASED ABSTRACT REACHABILITY ANALYSIS

In the proposed methodology the satisfaction of mission objectives is thus achieved via the maximization, over a given time horizon T_h, of a continuous functional $J(\mathbf{x})$ defined as

$$J(\mathbf{x}) = \sum_{i=1}^{n_{\Omega_i}} \int_{t_0}^{T_h} \omega_i(\mathbf{y}_i)\,d\tau = \sum_{i=1}^{n_{\Omega_i}} \int_{t_0}^{T_h} \omega_i(\mathbf{m}_i(\mathbf{x},\tau))\,d\tau \tag{4}$$

with n_{Ω_i} the number of observation regions considered and ω_i a set of continuous and differentiable activation functions that tend to one inside the observation region Ω_i and vanishes monotonically with increasing distance from it. In the current work this is achieved with the superposition of three sigmoid functions

$$\omega_i(\mathbf{y}_i) = \Psi_i(y_{i,1}) \cdot \Theta_i(y_{i,2}) \cdot \Upsilon_i(y_{i,3}) \tag{5}$$

with

$$\begin{aligned} \Psi_i(y_{i,1}) &= \frac{1}{1+e^{-K_1\left(y_{i,1}-\left(\frac{\rho_i^-}{\overline{R}}\right)^2\right)}} \cdot \frac{1}{1+e^{K_1\left(y_1-\left(\frac{\rho_i^+}{\overline{R}}\right)^2\right)}} \\ \Theta_i(y_{i,2}) &= \frac{1}{1+e^{-K_2\left(y_{i,2}-\cos(\theta_i^+)\right)}} \\ \Upsilon_i(y_{i,3}) &= \frac{1}{1+e^{-K_3\left(y_{i,3}-\cos(\beta_i^+)\right)}} \end{aligned} \tag{6}$$

The coefficients, K_1, K_2, and K_3, are tuning parameters used to control the decay rate of the sigmoid function outside the observation region.

Under the assumption of control affine dynamics, in the case of n_m impulsive maneuvers $\Delta\mathbf{v}_l$, executed at times t_l, the equation of motion for the spacecraft can be expressed as

$$\dot{\mathbf{x}} = \mathbf{f}_D(\mathbf{x}(t),t) + \mathbf{B}\sum_{l=1}^{n_m} \delta(t-t_l)\,\Delta\mathbf{v}_l \tag{7}$$

with $\mathbf{f}_D$ the dynamical drift describing the ballistic evolution of the trajectory, $\mathbf{B}$ the control input matrix and $\delta(\cdot)$ the Dirac delta function. The solution $\mathbf{x}(t)$ of Equation (7) is constrained to belong to the feasible set $\mathcal{X}$ defined as the envelope of trajectories that satisfy impact and escape constraints

$$\mathcal{X} := \{\mathbf{x} \in \mathbb{R}^6 \mid R_I \leq ||\mathbf{L}_r\mathbf{x}|| \leq R_E\} \tag{8}$$

where R_I and R_E refers respectively to an impact and an escape distance from the asteroid. Control constraints are instead imposed by bounding the $\Delta\mathbf{v}_l$, i.e. $\Delta\mathbf{v}_l \in \mathcal{U}$ with

$$\mathcal{U} := \{\Delta\mathbf{v}_l \in \mathbb{R}^3 \mid ||\Delta\mathbf{v}_l|| \leq \Delta v_{max}\} \tag{9}$$

where Δv_{max} is given by the actuators capacity.

The maximization of functional in Equation (4) subject to this set of constraints results hard to track on-board. A sub-optimal solution can however be found by dividing the problem into a sequence of trajectory planning problems $\mathcal{P}_j$, each defined over the time interval $[t_j, t_{j+1}]$ and allowing for a single burn $\Delta\mathbf{v}_j$ at t_j. An additional constraint is then needed so that the next maneuvering epoch t_{j+1} satisfies $t_{j+1} \in \mathcal{T}_j$, with

$$\mathcal{T}_j := \{t_{j+1} \mid t_j + \Delta t_{nav} \leq t_{j+1} \leq T_{hj}\} \tag{10}$$

where $T_{hj} < T_h$ and Δt_{nav} is a time interval designed to ensure enough time between subsequent maneuvers to let the on-board navigation filter converge.

The optimization scheme, initialized with problem $\mathcal{P}_0$, at t_0, and ending with problem $\mathcal{P}_f$, at T_h, is illustrated in Figure 4 where the minus suffix indicates the state before maneuver.

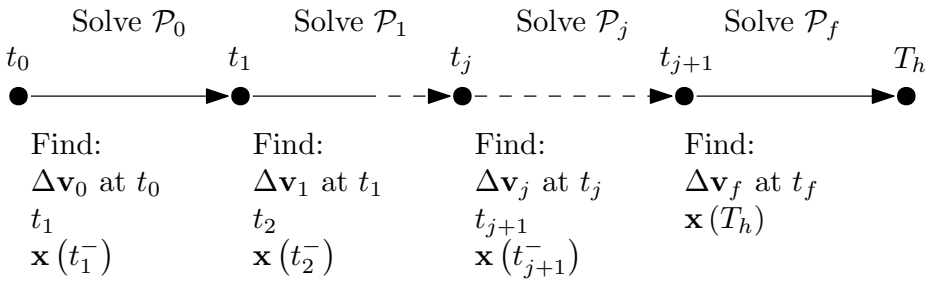

Figure 4: Sequential planning strategy.

Furthermore, control constraints can be imposed by augmenting the objective function J with a wall function $V_C(\mathbf{x})$ defined as

$$V_C(\mathbf{x}) = -\left(\frac{K_{I,1}}{1 + e^{K_{I,2}(||\mathbf{L}_r\mathbf{x}|| - R_I)}} + \frac{K_{E,1}}{1 + e^{-K_{E,2}(||\mathbf{L}_r\mathbf{x}|| - R_E)}}\right) \tag{11}$$

where $K_{I,1}$, $K_{I,2}$ and $K_{E,1}$, $K_{E,2}$ are tuning parameters associated respectively with the shape of the impact and escape potential.

The optimization problem can thus be formulated as

$$\begin{aligned}
&\max_{\Delta\mathbf{v}_j, t_{j+1}} J^A = \quad \frac{1}{T_{hj}} \int_{t_j}^{t_{j+1}} \left(\sum_{i=1}^{n_{\Omega_i}} \omega_i \left(\mathbf{m}_i \left(\mathbf{x}, \tau \right) \right) + V_C \left(\mathbf{x} \right) \right) d\tau \qquad \text{subject to:} \\
&\dot{\mathbf{x}} = \mathbf{f}_D \left(\mathbf{x} \left(t \right), t \right) \qquad \forall t \in [t_j, t_{j+1}] \\
&\mathbf{x} \left(t_j \right) = \mathbf{x} \left(t_j^- \right) + \mathbf{B} \Delta\mathbf{v}_j \\
&\Delta\mathbf{v}_j \in \mathcal{U} \\
&t_{j+1} \in \mathcal{T}_j
\end{aligned} \tag{12}$$

Instead of solving the optimal control problem in Equation (12) by sampling the control domain $\mathcal{U}$, similarly to what done by Surovik,[12] the proposed methodology aims at following the gradient of J^A, i.e

$$\nabla J^A \left(\Delta\mathbf{v}_j, t_{j+1} \right) = \left[\frac{\partial J^A}{\partial t_{j+1}}, \frac{\partial J^A}{\partial \Delta\mathbf{v}_j} \right]^T \tag{13}$$

It can be shown[19] that simply by inspecting the behavior of $J^A \left(\Delta\mathbf{v}_j, t \right)$ a criterion can be found to define for each value of $\Delta\mathbf{v}_j$ the best epoch to locate the subsequent maneuver t_{j+1}. This can be used as a black box to define the relation $t_{j+1} \left(\Delta\mathbf{v}_j \right)$ thus reducing the dimensionality of the problem from four to three dimensions. In fact, starting from an initial guess $\Delta\mathbf{v}_j^{(0)}$, an iterative gradient ascend technique can be put in place such that the iteration

$$\Delta\mathbf{v}_j^{(k+1)} = \Delta\mathbf{v}_j^{(k)} + \alpha_k \hat{\mathbf{d}}^{(k)} \left(\frac{\partial J^A}{\partial \Delta\mathbf{v}_j} \right) \tag{14}$$

converges to a local maximum of J^A with proper selection[19] of the step α_k and ascend direction $\hat{\mathbf{d}}^{(k)}$. The gradient $\dfrac{\partial J^A}{\partial \Delta\mathbf{v}_j}$ can be computed differentiating J^A as

$$\frac{\partial J^A}{\partial \Delta\mathbf{v}_j} = \frac{1}{T_{hj}} \int_{t_j}^{t_{j+1}} \left(\sum_{i=1}^{n_{\Omega_i}} \frac{\partial \omega_i}{\partial \mathbf{y}_i} \frac{\partial \mathbf{y}_i}{\partial \mathbf{x}} + \frac{\partial V_C}{\partial \mathbf{x}} \right) \mathbf{\Phi}(\tau, t_j) \mathbf{B} d\tau \tag{15}$$

with $\mathbf{\Phi}(\tau, t_j)$ being the State Transition Matrix (STM), from epoch t_j to epoch τ computed integrating the variational equations[20]

$$\dot{\Phi} \left(\tau, t_j \right) = \frac{\partial \mathbf{f}_D \left(\mathbf{x}, t \right)}{\partial \mathbf{x}} \Phi \left(\tau, t_j \right) \tag{16}$$

with the initial condition $\Phi \left(t_j, t_j \right) = \mathbf{I}_{6\times 6}$. To increase the chance of converging to global optima the Gradient Based Reachability (GBR) scheme is alternated with sampling based ramifications in the neighboured of the solution found stopping the iterations only when $\Delta\mathbf{v}_j$ or J^A variation fall below a specified threshold.[19]

4 TRAJECTORY REFINEMENT WITH SEQUENTIAL CONVEX PROGRAMMING

The deterministic trajectory $\mathbf{x}_D(t)$ generated with abstract reachability analysis is then refined using SCP. A simplified cost function J_P to be minimized is defined in this case as a linear combination of the spacecraft square distances from the center $\mathbf{r}_{\Omega_i^P}$ of the spherical sectors Ω_i^P at specific observation epochs t_i^*

$$J_P(\mathbf{r}_\mathcal{B}) = \sum_{i=1}^{n_{\Omega_i}} w_i^* \left(\mathbf{r}_\mathcal{B}(t_i^*) - \mathbf{r}_{\Omega_i^P}\right)^T \left(\mathbf{r}_B(t_i^*) - \mathbf{r}_{\Omega_i^P}\right) \tag{17}$$

with t_i^* computed as the time at which the distance from the region Ω_i^P is minimized on the deterministic trajectory $\mathbf{x}_D(t)$

$$t_i^* = arg\min_t \left(d^2_{\Omega_i^P}(\mathbf{x}_D(t))\right) \tag{18}$$

ensuring the satisfaction of illumination requirements. As illustrated in Figure 5, this distance is computed as

$$d_{\Omega_i^P}(t) := ||\mathbf{r}_\mathcal{B} - \mathbf{s}_{P,\Omega_i^P}|| \tag{19}$$

where $\mathbf{s}_{P,\Omega_i^P}$ is the projection of the spacecraft position on the set Ω_i^P. By exploiting a proper change of variables, the quantity $d^2_{\Omega_i^P}$ can be computed analytically in closed form,[16] avoiding solving a separate convex optimization problem.[21]

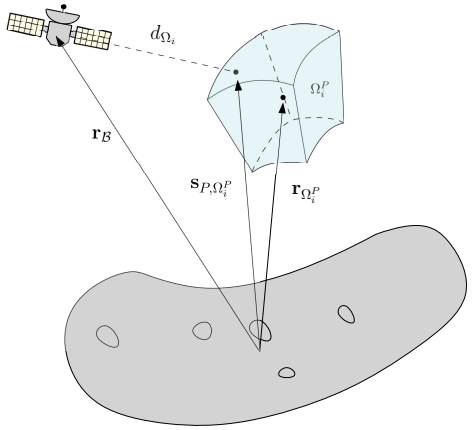

Figure 5: Schematic representation of the projection problem.

Finally, expressing the cost function in terms of spacecraft state and neglecting the constant terms leads to the following optimization problem

$$
\begin{aligned}
&\min_{\Delta \mathbf{v}_l} \quad \sum_{i=1}^{n_{\Omega_i^P}} w_i^* \left(\mathbf{x}^T \left(t_i^* \right) \mathbf{L}_{rr} \mathbf{x} \left(t_i^* \right) + \mathbf{q}_{i,P}^T \left(t_i^* \right) \mathbf{x} \left(t_i^* \right) \right) \qquad \text{subject to:} \\
&\dot{\mathbf{x}} = \mathbf{f}_D \left(\mathbf{x} \left(t \right), t \right) + \mathbf{B} \sum_{l=1}^{n_m} \delta \left(t - t_l \right) \Delta \mathbf{v}_l \qquad \forall t, t_l \in [t_0, T_h] \\
&\mathbf{x} \left(t_0 \right) = \mathbf{x}_0 \\
&||\mathbf{L}_r \mathbf{x}|| \geq R_I \qquad \forall t \in [t_0, T_h] \\
&-R_E \mathbf{I}_{3\times 1} \leq \mathbf{L}_r \mathbf{x} \leq R_E \mathbf{I}_{3\times 1} \qquad \forall t \in [t_0, T_h] \\
&||\Delta \mathbf{v}_l|| \leq \Delta v_{max} \qquad \forall l \in [1, n_m]
\end{aligned}
\tag{20}
$$

with $\mathbf{q}_{i,P} \left(t \right) = -2\mathbf{L}_r^T \mathbf{R}_{\mathcal{N}2\mathcal{B}}^T \left(t \right) \mathbf{r}_{\Omega_i^P}$ related with the motion of the observation region Ω_i^P in the inertial frame $\mathcal{N}$. Also note that the escape constraint in Equation (8) is relaxed in an upper and lower bound constraints to reduce the complexity of the problem. To solve the problem in Equation (20) with SCP the non-linear dynamics and the impact constraints needs to be sequentially convexified in the neighboured of the previous step solution $\hat{\mathbf{x}}(t)$, $\Delta \hat{\mathbf{v}}_l$. The former is achieved via linearization and discretization over a fine temporal grid

$$
\begin{aligned}
&\delta \mathbf{x}_1 = \mathbf{0}_{3\times 1} \\
&\delta \mathbf{x}_k = \mathbf{\Phi}(t_k, t_{k-1}) \delta \mathbf{x}_{k-1} + \mathbf{\Phi}(t_k, t_{k-1}) \mathbf{B} \delta \Delta \mathbf{v}_{k-1} \quad \forall k = 2, ..., n_t
\end{aligned}
\tag{21}
$$

with $\delta \mathbf{x}(t) = \mathbf{x}(t) - \hat{\mathbf{x}}(t)$, $\delta \Delta \mathbf{v}_l = \Delta \mathbf{v}_l - \Delta \hat{\mathbf{v}}_l$ and n_t the number of nodes. To enforce the validity of the linearization a trust region constraint needs to be imposed bounding the maximum deviation from the reference trajectory

$$
||\delta \mathbf{x}(t)||_1 = \sum_{j=1}^{6} |\delta x_k^{(j)}| \leq R \quad \forall k = 2, ..., n_t \tag{22}
$$

with $R \in \mathbb{R}$ and the superscript j indicating the vector component. The impact condition $||\mathbf{L}_r \mathbf{x}|| \geq R_I$ can be instead relaxed with half-spaces approximations in the neighborhood of the previous iteration[22,23] as

$$
\hat{\mathbf{r}}_k^T \mathbf{r}_k \geq R_I ||\hat{\mathbf{r}}_k|| \implies -\hat{\mathbf{x}}_k^T \mathbf{L}_r^T \mathbf{L}_r \mathbf{x}_k \leq -R_I ||\mathbf{L}_r \hat{\mathbf{x}}_k|| \quad \forall k = 1, ..., n_t \tag{23}
$$

To ensure theoretical consistency to counteract artificial infeasibility,[23] additional variables $\boldsymbol{\nu}_k \in \mathbb{R}^6$ and $\xi_k \geq 0$ are added to the dynamic constraint and to the impact constraint and known respectively as virtual control and virtual buffer. At the final iteration of the SCP these additional slacks have to be close to zero, to induce this they are added in the cost function pre-multiplied by large constants M_D and M_I.

Finally, in order to get rid of the quadratic terms in the cost function and transform the problem into a Second Order Cone Program (SOCP), suitable to most solvers, a set of slack variables s_i is introduced together with an additional inequality constraint. The convex optimization problem thus becomes

$$
\begin{aligned}
&\min_{\Delta\mathbf{v}_l} \quad \sum_{i=1}^{n_{\Omega_i^P}} w_i^* \left(s_i + \mathbf{q}_{i,Pi}^T \mathbf{x}_i\right) + M_D \sum_{k=1}^{n_t} ||\boldsymbol{\nu}_k||_1 + M_I \sum_{k=1}^{n_t} |\xi_k| && \text{subject to:} \\
&\delta\mathbf{x}_1 = \mathbf{0}_{3\times 1} \\
&\delta\mathbf{x}_k = \boldsymbol{\Phi}(t_k, t_{k-1})\delta\mathbf{x}_{k-1} + \boldsymbol{\Phi}(t_k, t_{k-1})\mathbf{B}\delta\Delta\mathbf{v}_{k-1} + \boldsymbol{\nu}_k && \forall k = 2, ..., n_t \\
&-\hat{\mathbf{x}}_k^T \mathbf{L}_r^T \mathbf{L}_r \mathbf{x}_k + R_I ||\mathbf{L}_r \hat{\mathbf{x}}_k|| \leq \xi_k && \forall k = 1, ..., n_t \\
&\xi_k \geq 0 && \forall k = 1, ..., n_t \\
&-R_E \mathbf{I}_{3\times 1} \leq \mathbf{L}_r \mathbf{x}_k \leq R_E \mathbf{I}_{3\times 1} && \forall k = 1, ..., n_t \\
&||\Delta\mathbf{v}_k|| \leq \Delta v_{max} && \text{with } k = l \\
&\Delta\mathbf{v}_k = \mathbf{0}_{3\times 1} && \text{with } k \neq l \\
&||\delta\mathbf{x}_k||_1 \leq R && \forall k = 2, ..., n_t \\
&\mathbf{x}_i^T \mathbf{L}_{rr} \mathbf{x}_i \leq s_i && \forall i = 1, ..., n_{\Omega_i^P}
\end{aligned}
\tag{24}
$$

Navigation and control uncertainties are taken into account in this optimization in three separate steps. First of all the state covariance at the maneuvering nodes $\mathbf{P}(t_l)$ is modelled as

$$
\mathbf{P}(t_l) = \begin{bmatrix} \mathbf{P}_{rr}^N(t_l) & \mathbf{P}_{rv}^N(t_l) \\ \mathbf{P}_{rv}^{NT}(t_l) & \mathbf{P}_{vv}^N(t_l) + \mathbf{P}_{vv}^C(\Delta\mathbf{v}_l) \end{bmatrix} \tag{25}
$$

with $\mathbf{P}_{rr}^N$, $\mathbf{P}_{vv}^N$ and $\mathbf{P}_{rv}^N$ describing the estimated position, velocity and cross-correlated covariance, and $\mathbf{P}_{vv}^C$ the velocity covariance due to control uncertainty and modeled as described by Laurens et al.[24] In particular, let us consider a thruster reference frame $\mathcal{T}$ centered in the spacecraft center of mass and oriented with the X axis in the direction of thrust, as shown in Figure 6.

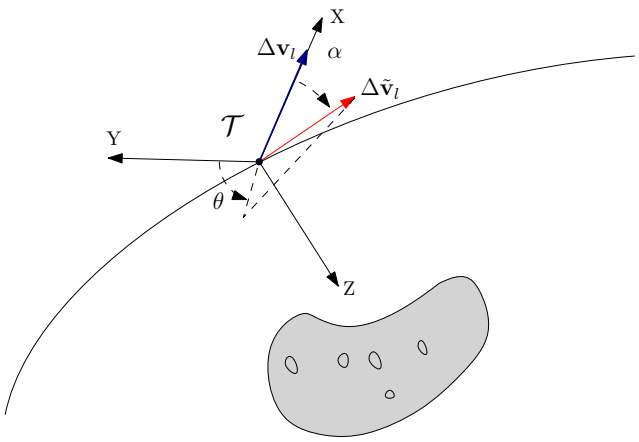

Figure 6: Sketch showing reference frame $\mathcal{T}$ and firing errors.

The realization $\Delta\tilde{\mathbf{v}}_l$ of the guidance solution $\Delta\mathbf{v}_l$, in this reference frame can be expressed as

$$\Delta\tilde{\mathbf{v}}_{l,\mathcal{T}} = (1+m_\epsilon)\,\Delta v_l \begin{bmatrix} cos(\alpha) \\ sin(\alpha)cos(\theta) \\ sin(\alpha)sin(\theta) \end{bmatrix} \tag{26}$$

where $m_\epsilon \in \mathcal{N}(0,\sigma_m)$ is the magnitude error while $\alpha \in \mathcal{N}(0,\sigma_d)$ and $\theta \in \mathcal{U}(-\pi,\pi)$ define the misalignment. The variable Δv_l refers instead to $||\Delta\mathbf{v}_l||$. It can be shown[24] that the control covariance, in Equation (25), in the thruster reference frame can be computed as

$$\mathbf{P}^C_{vv,\mathcal{T}}(\Delta\mathbf{v}_l) = \begin{bmatrix} 2N\left(1+P^2\right) - P\Delta v_l^2 & 0 & 0 \\ 0 & N\left(1-P^2\right) & 0 \\ 0 & 0 & N\left(1-P^2\right) \end{bmatrix} \tag{27}$$

with $N = \frac{1}{4}\left(1+\sigma_m^2\right)\Delta v_l^2$ and $P = e^{-\sigma_d^2}$. Combining Equation (25), with Equation (27) leads to

$$\mathbf{P}(t_l) = \begin{bmatrix} \mathbf{P}^N_{rr} & \mathbf{P}^N_{rv} \\ \mathbf{P}^{NT}_{rv} & \mathbf{P}^N_{vv} + \mathbf{R}_{\mathcal{T}2\mathcal{N}}\mathbf{P}^C_{vv,\mathcal{T}}\mathbf{R}^T_{\mathcal{T}2\mathcal{N}} \end{bmatrix} \tag{28}$$

and $\mathbf{R}_{\mathcal{T}2\mathcal{N}}$ is the rotation matrix from the thruster frame to the inertial reference frame.

Uncertainty is thus linearly propagated to the observation epochs t_i^* to retrieve the estimated dispersion in the form of the position covariance $\mathbf{P}_{rr}(t_i^*)$.

$$\begin{aligned} \mathbf{P}_{rr}(t^*) =& \mathbf{\Phi}_{rr}(t^*,t_l)\,\mathbf{P}_{rr}(t_l)\,\mathbf{\Phi}^T_{rr}(t^*,t_l) + \mathbf{\Phi}_{rv}(t^*,t_l)\,\mathbf{P}_{vv}(t_l)\,\mathbf{\Phi}^T_{rv}(t^*,t_l) + \\ &+2\mathbf{\Phi}_{rr}(t^*,t_l)\,\mathbf{P}_{rv}(t_l)\,\mathbf{\Phi}^T_{rv}(t^*,t_l) \end{aligned} \tag{29}$$

Regions Ω_i^P are then scaled down by a factor Γ_i associated with the spectral radius of $\mathbf{P}_{rr}$ at t_i^*

$$\Gamma_i = \frac{R_{\Omega_i^P} - 3\sigma_r^{\max}(t_i^*)}{R_{\Omega_i^P}} \tag{30}$$

where $R_{\Omega_i^P}$ is the size of Ω_i^P and $\sigma_r^{\max}(t_i^*) = \sqrt{\lambda^{max}(\mathbf{P}_{rr}(t_i^*))}$. This ensures that the trajectory crosses the region even under uncertainties with a 99% confidence level assuming a Gaussian distribution, see Figure 7.

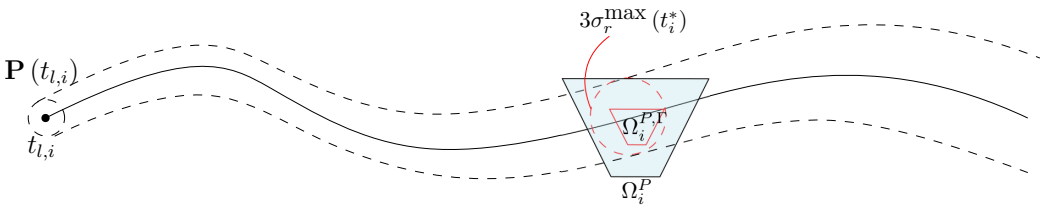

Figure 7: Observation regions contraction scheme.

A closed form analytical solution derived by the author[16] is used to impose an upper bound to maneuver magnitude depending on navigation and control uncertainties needed to keep the standard deviation of the position below a desired value σ_r^{toll}. This replaces the control constraint with

$$\Delta v_l \leq \sqrt{\frac{1}{\chi\left(\sigma_m, \sigma_d\right)}\left[\frac{\left(\sigma_r^{\text{toll}}\right)^2 - \lambda^{max}\left(\mathbf{\Phi}_{rr}\mathbf{\Phi}_{rr}^T\right)\left(\sigma_r^N\left(t_l\right)\right)^2 - \left[\sigma_{rv}^P\left(t_l\right)\right]^2}{\lambda^{max}\left(\mathbf{\Phi}_{rv}\mathbf{\Phi}_{rv}^T\right)} - \left(\sigma_v^N\left(t_l\right)\right)^2\right]} \tag{31}$$

with

$$\sigma_r^N = \sqrt{\lambda^{\max}\left(\mathbf{P}_{rr}^N\right)}, \quad \sigma_v^N = \sqrt{\lambda^{\max}\left(\mathbf{P}_{vv}^N\right)} \tag{32}$$

$$\sigma_{rv}^P = \sqrt{\lambda^{\max}\left(2\mathbf{\Phi}_{rr}\left(t^*, t_l\right)\mathbf{P}_{rv}^N\left(t_l\right)\mathbf{\Phi}_{rv}^T\left(t^*, t_l\right)\right)} \tag{33}$$

For simplicity, in the results discussed in Section 6 this latter term associated with cross correlation is neglected assuming diagonal $\mathbf{P}(t_l)$. Finally, weighting factors w_i^* in the cost functions are changed according to the contraction factor Γ_i as

$$w_i^* = 2 - \Gamma_i \tag{34}$$

5 AUTONOMOUS GOAL-ORIENTED FRAMEWORK

The two methodologies described in this paper are combined in the proposed goal-oriented guidance algorithm illustrated in Figure 8.

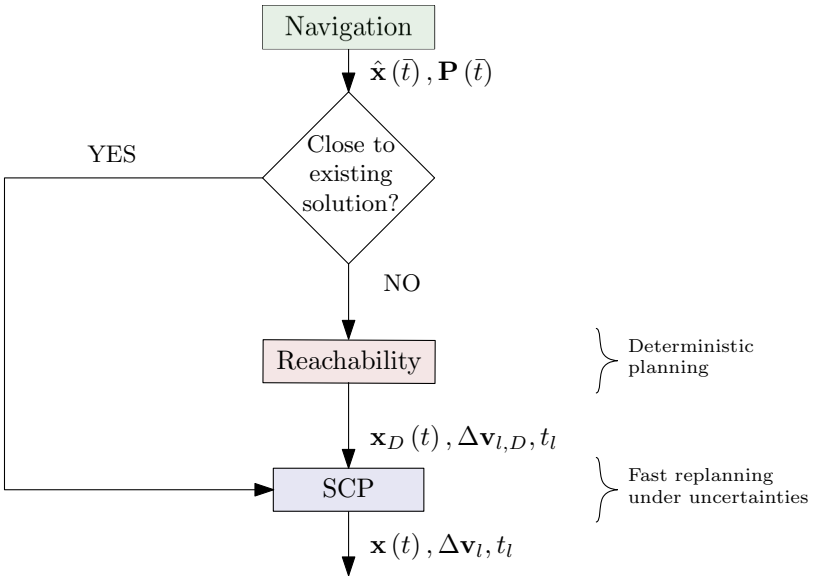

Figure 8: GNC functional workflow.

When the guidance algorithm is called at a given epoch $\bar{t}$ the estimated spacecraft state $\hat{\mathbf{x}}$ and and error covariance $\mathbf{P}$ are retrieved from an on-board navigation algorithm. For the demonstration

presented in the next section, surrogate navigation models are used with assumed performances at the planning epochs. If the estimated state is far from an already existing guidance solution, or if no solution exists, reachability analysis and SCP are executed in series. Otherwise only the SCP scheme is used to perform fast replanning of the previously planned trajectory under navigation and control uncertainties.

This GNC algorithm is embedded within a model predictive control scheme that triggers the algorithm at specified epochs. For the test case shown in the next section the GNC pipeline is always called 5 minutes before the execution of a maneuver. For this work the full algorithm is written in MATLAB2022a and the SCP part is solved by means of CVX*[25] using the SEDUMI[26] solver. The full pipeline described so far is tested in a high fidelity simulation environment with surrogate models for navigation algorithms and actuators to properly simulate navigation and control uncertainties. A truth model different with respect to the one used on-board is used to simulate the effect of unmodelled dynamics due non-uniform gravity distribution.[27] A test case showing the effectiveness of the algorithm is shown in the next section.

6 CASE STUDY - EROS PROXIMITY OPERATIONS

This section presents a case study to prove the proposed methodology. Asteroid (433) Eros is selected as the target to be observed with the mission goal driven by the observation of 10 features on the surface as shown in Figure 9. The proposed scenario assumes an initial epoch t_0 corresponding to 2000 AUG 01 12:00 (UTC) such that quite uniform illumination conditions are obtained avoiding observability issues.

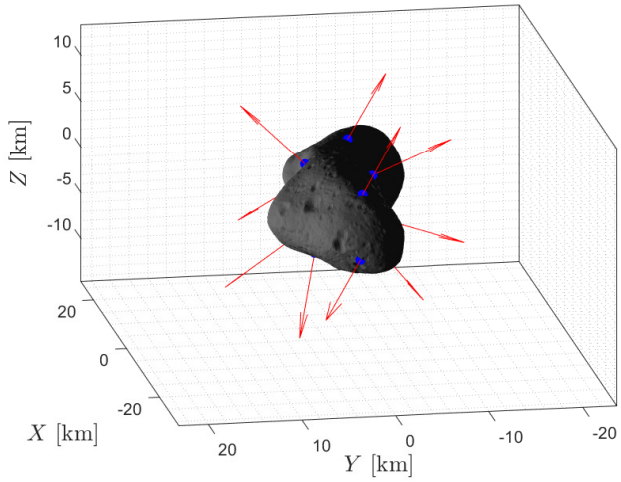

Figure 9: Mission goal considered for the Eros case study. Blue dots indicates the features position $\mathbf{r}_{i\mathcal{B}}$, while red arrows refers to the local normal to the surface $\mathbf{n}_{i\mathcal{B}}$.

Referring to Figure 2, for each feature the observation requirements are defined by $\rho_i^+ = 40$ km, $\rho_i^- = 35$ km, $\theta_i^+ = 15$ deg and $\beta_i^+ = 90$ deg. GBR and SCP tuning parameters introduced in this paper are summarized respectively in Tables 1 and 2.

Table 1: Configuration parameters for the GBR scheme.

Variable	Description	Value
K_1	V coefficient, Equation (6)	100
K_2	V coefficient, Equation (6)	100
K_3	V coefficient, Equation (6)	100
$\overline{R}$	$y_{i,1}$ scaling, Equation (2)	16 km
$K_{I,1}$	V_C coefficient, Equation (11)	1
$K_{I,2}$	V_C coefficient, Equation (11)	4
$K_{E,1}$	V_C coefficient, Equation (11)	1
$K_{E,2}$	V_C coefficient, Equation (11)	4
R_I	Impact radius, Equation (8)	24 km
R_E	Escape radius, Equation (8)	100 km
Δv_{max}	Maximum control, Equation (9)	2 m/s
T_{hj}	Problem $\mathcal{P}_j$ horizon, Equation (10)	12 h
Δt_{nav}	Navigation margin, Equation (10)	1 h

Table 2: Configuration parameters for the SCP scheme.

Variable	Description	Value
σ_r^N	Position uncertainty, Equation (31)	10 m
σ_v^N	Velocity uncertainty, Equation (31)	10 mm/s
σ_m	Magnitude uncertainty, Equation (31)	0.0167 (5 %, 3 σ)
σ_d	Misalignment uncertainty, Equation (31)	0.667 deg (2 deg, 3 σ)
$\tilde{\Gamma}_i$	Minimum contraction, Equation (30) with σ_r^{toll}	0.7
$R_{(0)}$	Initial trust region, Equation (22)	0.1
M_D	Virtual control weight, Problem (24)	100
M_I	Virtual buffer weight, Problem (24)	100

The system dynamics is modeled considering the effect of spherical and non-spherical central gravity field with the drift term in Equation (7) computed as

$$\mathbf{f}_D\left(\mathbf{x}\right) = \begin{bmatrix} \mathbf{v} \\ \mathbf{R}_{\mathcal{N}2\mathcal{B}}^T \nabla U \end{bmatrix} \tag{35}$$

with U begin the gravitational potential. Solar radiation pressure and third body effects are shown to be negligible when operating at this range from Eros.[16] To model the effect on dynamic uncertainties a difference is introduced in the modeling of U for the on-board computation and the environment propagation. Both models are based on a spherical-harmonic expansion of the gravity field up to order 10. However, the on-board potential is computed assuming a uniform density distribution with $\rho_{Eros} = 2670$ kg/m^3 while the dynamics in the environment consider the case of a variable density asteroid with heavier inner core with density

$$\rho(\mathbf{r}) = \begin{cases} \rho_1 = 2937 \text{ kg/m}^3 & r \leq 5 \text{ km} \\ \rho_2 = 2670 \text{ kg/m}^3 & r > 5 \text{ km} \end{cases} \tag{36}$$

To model this, a pipeline developed by the author is used[27] to efficiently map generic density distribution defined over a polyhedral shape model to the coefficients of spherical harmonics.

A Monte Carlo analysis is performed over the initial conditions and uncertainties realizations to statistically characterize the performances of the algorithm. The samples of 100 initial states used in the MC is shown in Figure 10.

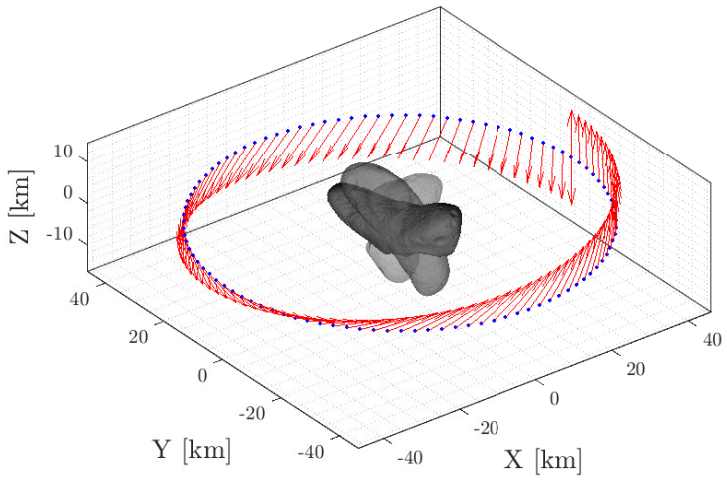

Figure 10: Initial conditions for the MC analyses. Blue dots and red arrows refer to initial position and velocity vectors, respectively.

A dataset with 10000 sample per random variable is generated based on the parameters specified in Table 2, the point cloud for position and velocity deviation is shown in Figure 11 while magnitude and misalignment errors are reported in Figure 12. The 10000 samples are clustered in groups of 100 and each group is associated with a different instance of the MC. This allows to always have a different but known random sequence both for navigation and control.

Performances are assessed in terms of goal satisfaction, overall Δv budget and percentage of success. The goal, in particular, is expressed through the variable g equal to the number of observation

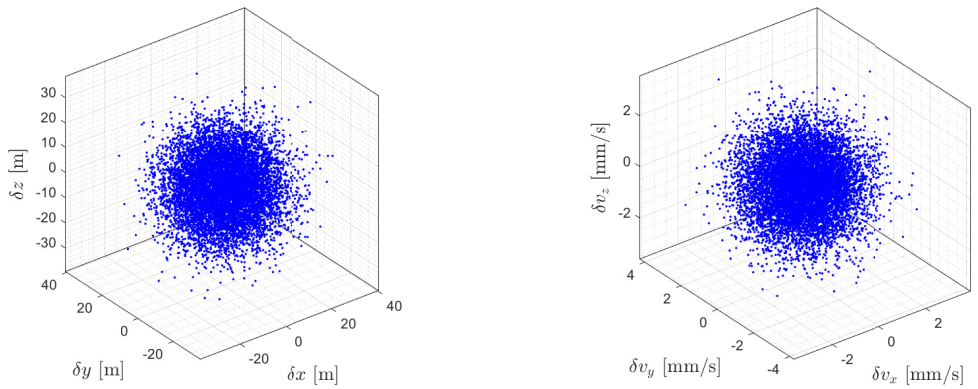

a b

Figure 11: (a) Position and, (b) velocity deviation samples used in the navigation surrogate model.

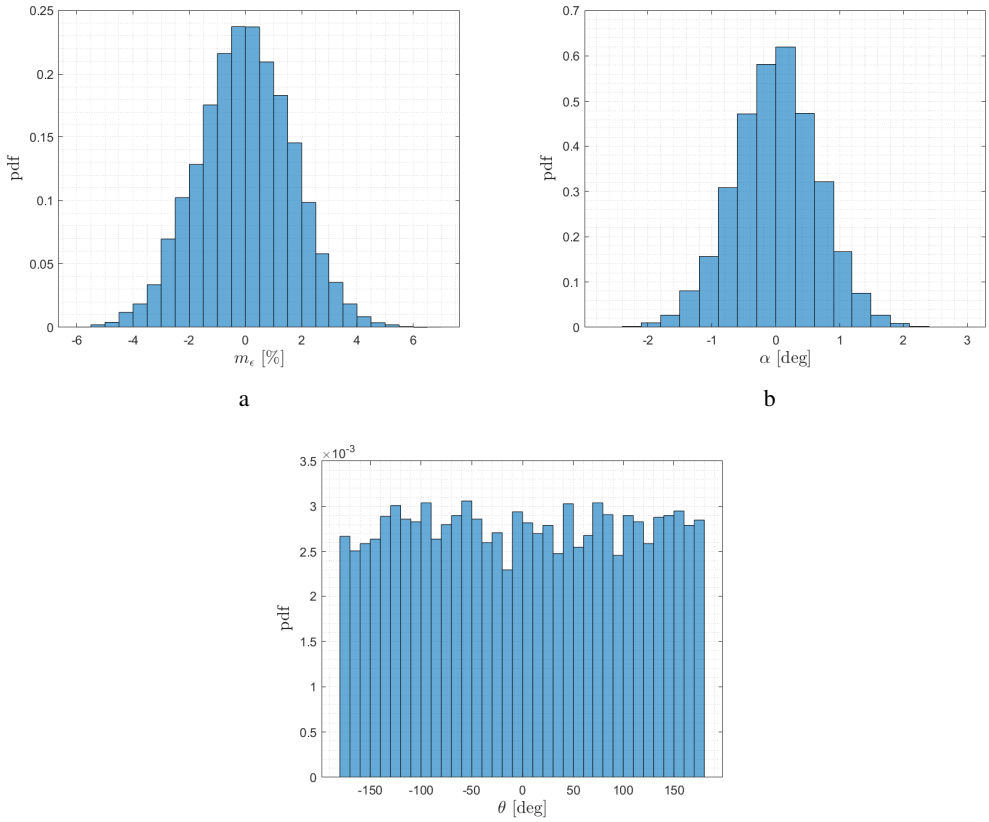

a b c

Figure 12: Control uncertainties samples used in the actuators surrogate model. (a) Magnitude uncertainties (in percentage), (b) α angle and, (c) θ angle.

regions that are observed. The simulated trajectory are grouped in four categories depending on their performance as summarized in Table 3 and results are discussed below.

Table 3: Classification used to cluster the solution of the MC analyses.

Classification	Goal range
Good coverage	$g \geq 7$
Low coverage	$g < 7$
Impact/Escape	$\mathbf{x}(t) \notin \mathcal{A}$ at a given $t > t_0$

Figure 13a shows the goal achieved by the 100 instances of the MC as a function of time, while Figure 13b reports the final values reached. Performances are summarized in Table 4

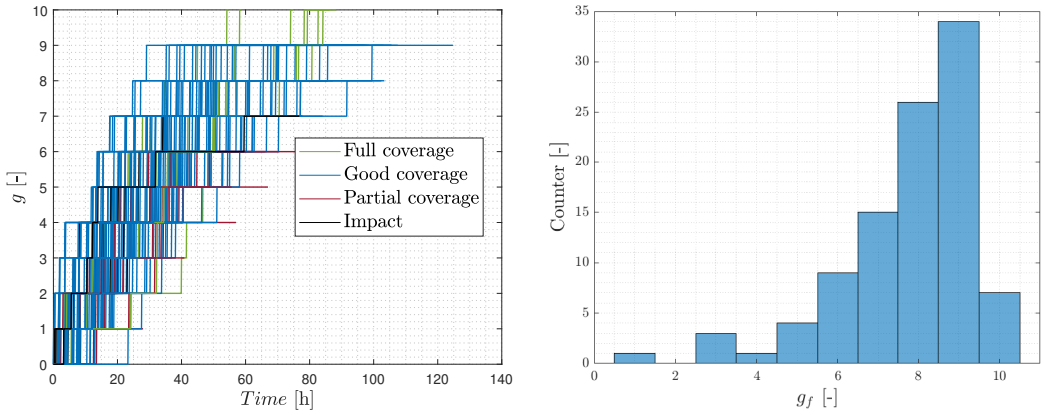

a b

Figure 13: Goal achievement with navigation, control and dynamic uncertainties. (a) Shows the evolution of $g(t)$ with the line colors indicating the achieved performance. (b) Illustrates an histogram of the final goal reached by each simulation.

Table 4: Overall performances with navigation, control and dynamics uncertainties included.

Classification	Percentage of samples
Good coverage	80 %
Low coverage	13 %
Impact/Escape	7 %

Good performances are achieved in the large majority of cases with an asymptotic convergence behavior, observed in the temporal evolution of the goal, that leads fewer cases with reduces performances. This is due to the potential-based nature of the reachability analysis with the gradient of J tending to zero when convergence is approached.

Figure 14 reports on an histogram the magnitude distribution of the $\Delta \mathbf{v}$s. The distribution can be approximated with a Gaussian probability function with mean at 16.45 m/s and standard deviation equal to 5.63 m/s.

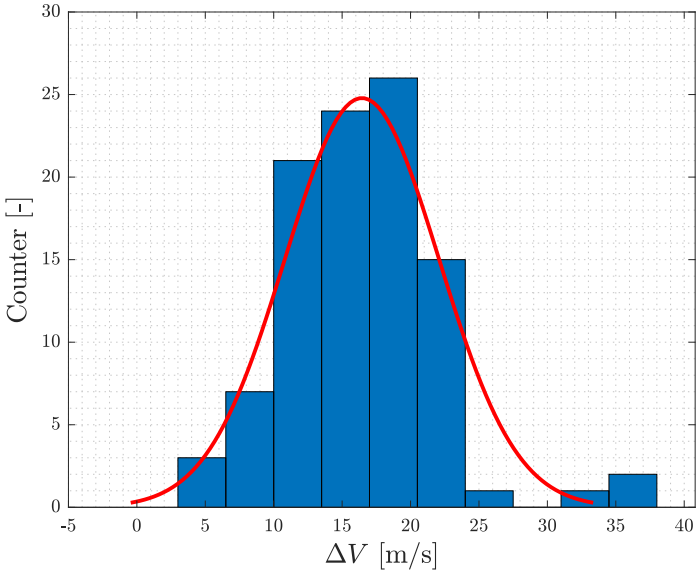

Figure 14: Histogram representing the statistical distribution of Δv budget for the mission with navigation, control and dynamics uncertainties.

A representative case is reported with initial conditions $\mathbf{r}_0 = [26.103, 36.656, 0]$ km and $\mathbf{v}_0 = [-1.187, 0.846, -2.823]$ m/s in the inertial frame $\mathcal{N}$. Figure 15 shows the optimal inertial and asteroid fixed trajectory with the regions Ω_i^P reported in the latter one showing that all observation regions are successfully crossed.

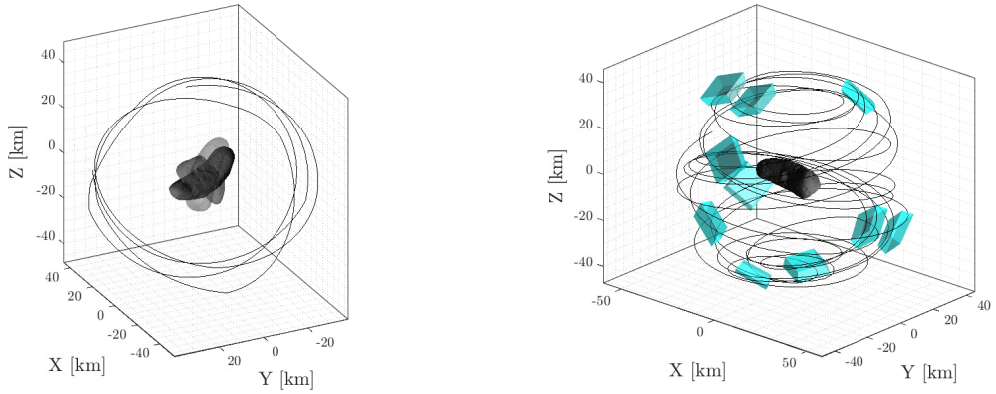

a b

Figure 15: Optimal trajectory for a full coverage case with navigation, control and dynamics uncertainties. (a) Trajectories in the inertial frame $\mathcal{N}$ and, (b) in the asteroid-fixed frame $\mathcal{B}$.

More insightful information on the algorithm performances can be deduced, as shown in Figure 16,

by comparing true range and velocity evolution (solid black lines), against the navigation solution (blue markers) and the state predicted by the guidance algorithm (red markers). Markers also corresponds to the epochs at which the MPC algorithm is triggered. The green vertical lines mark the epochs at which observation regions are crossed.

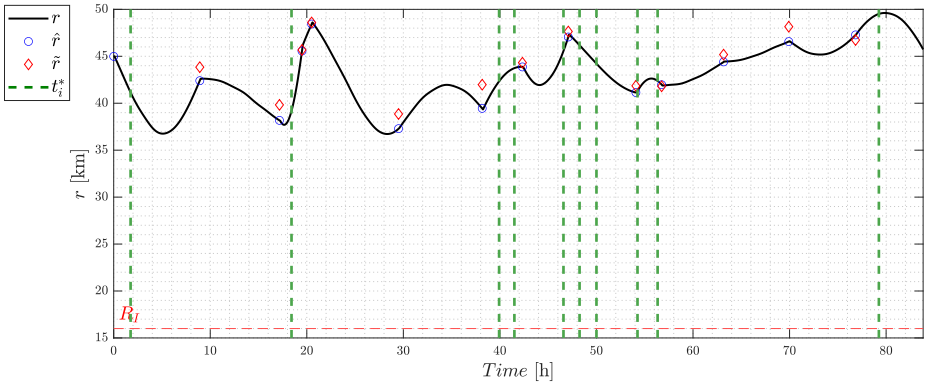

a

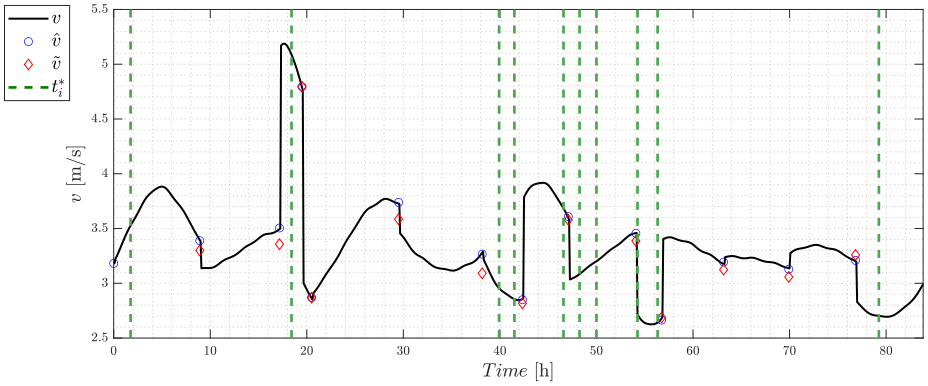

b

Figure 16: Trajectory temporal evolution for the considered case with navigation, control and dynamics uncertainties. (a) Spacecraft range as a function time. (c) Spacecraft velocity as a function of time.

The difference between the predicted trajectory and the real one is the so called dispersion. In the case discussed here, navigation, control and dynamic uncertainties induce large dispersion but the proposed guidance pipeline is capable of compensating for them and complete the observation tasks.

For comparison, the same instance of the Monte Carlo is performed using only the deterministic path planning as shown in Figure 17. The simulation shows that higher peaks in the dispersion occur, and the trajectory ends before completing the coverage.

Impacts instead, are mainly due to the fact that the trajectory predicted by the algorithm significantly deviate from the real one in a way the MPC strategy, in its current implementation, is not capable of compensating. This is due to a combination of factors: 1) the guidance solution is

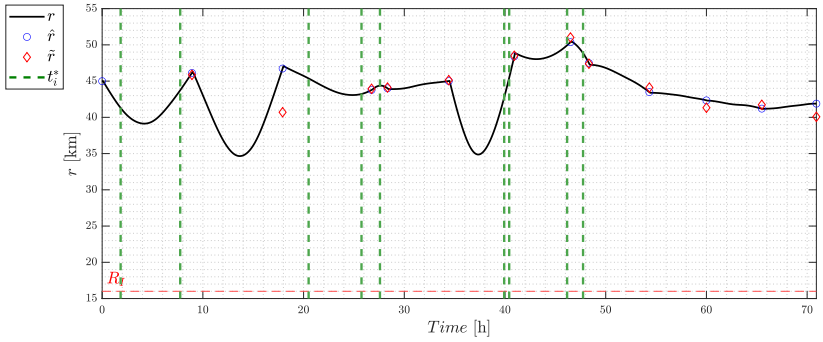

a

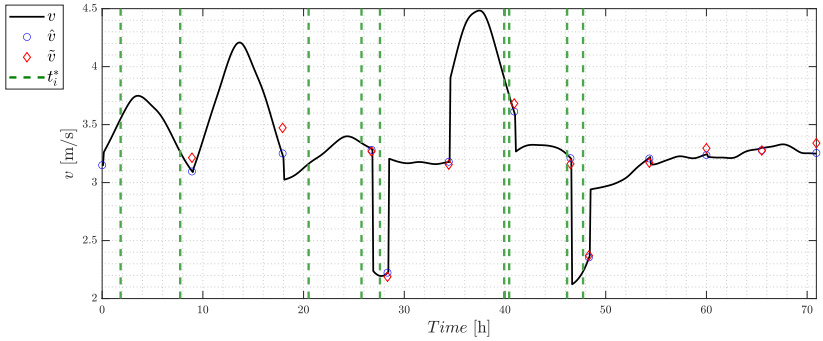

b

Figure 17: Trajectory temporal evolution for the considered case with navigation, control and dynamics uncertainties without SCP refinement. (a) Algorithm used to compute the guidance profile during the different GNC calls. (b) Spacecraft range as a function time. (c) Spacecraft velocity as a function of time.

computed starting from an estimated spacecraft state with accuracy depending on navigation performances, 2) the interaction between control uncertainties and maneuvers magnitudes resonates with the small bodies chaotic environment generating large dispersion over short time windows, 3) the partial knowledge of the operative environment further enhance all these effects. Possible improvements in this direction could be achieved by taking into account chaos indicators, such as the Fast Lyapunov Indicators (FLI),[28] the spectral radius of the Cauchy Green tensor used in this work, or more recent concepts, such as the Lagrangian Descriptors,[29] to locate maneuvers in less sensible regions similarly to what done by Oguri et al.[30] Moreover, dynamics uncertainties could also be embedded in the uncertainty propagation of Equation (29) by adding some process noise.[31,32]

7 CONCLUSIONS

In this work, a gap is identified between the current development of deep-space CubeSats, willing to accept bigger risks in sight of a higher reward, and the current level of autonomy available for this platforms. To cover this gap a two steps guidance pipeline is developed in which deterministic path planning is performed by means of gradient based reachability analysis and refined in an uncertainty robust framework with sequential convex programming. Additional robustness is added by framing this algorithm within a model predictive control logic. Results shows that good performances can

be achieved with the proposed methodology with more than 80% of the considered simulations achieving good coverage under navigation, control and dynamic uncertainties. Furthermore, the dispersion error achieved in the successful cases, performs similarly to relevant work in literature. Kuettel,[33] for example, proves a control accuracy of a few hundreds meters for low-thrust operations around small bodies, with similar navigation accuracy, 30 m and 5 mm/s at 3σ, but less conservative control errors, 1% in magnitude. Overall this paper propose a guidance strategy for goal-oriented operations around small bodies representing thus a step forward towards autonomous GNC for deep-space exploration missions.

APPENDIX - NOTATION

In this work two reference frames are defined:

- **Inertial reference frame** $\mathcal{N}$: origin in the center of mass of the target and oriented as ECLIPJ2000
- **Asteroid fixed frame** $\mathcal{B}$: origin in the center of mass of the target and aligned with the principal inertia axes of the target

The following conventions are adopted for the notation:

- reference frames are indicated with upper case calligraphic letters ($\mathcal{N}, \mathcal{B}$),
- plain text indicates scalar variables (t),
- bold letters in lowercase indicates column vectors ($\mathbf{x}, \mathbf{u}$),
- a vector $\mathbf{x}$ expressed in reference frame $\mathcal{A}$ is indicated as $\mathbf{x}_{\mathcal{A}}$,
- for simplicity of notation when a vector is expressed in the inertial reference frame $\mathcal{N}$ defined later in this section, its dependence is omitted ($\mathbf{x} = \mathbf{x}_{\mathcal{N}}$),
- bold letters in uppercase indicates matrices and tensors ($\mathbf{B}, \mathbf{\Phi}$),
- the identity matrix of size $n \times n$ is represented as $\mathbf{I}_{n\times n}$,
- the null matrix of size $n \times m$ is represented as $\mathbf{0}_{n\times m}$,
- the direction cosine matrix to rotate a vector from reference frame $\mathcal{A}$ to reference frame $\mathcal{B}$ is indicated as $\mathbf{R}_{\mathcal{A}2\mathcal{B}}$.

Two matrices are used several times across this dissertation, $\mathbf{L}_r$ and $\mathbf{L}_{rr}$ defined as

$$\mathbf{L}_r = \begin{bmatrix} \mathbf{I}_{3\times 3} & \mathbf{0}_{3\times 3} \end{bmatrix} \tag{37}$$

$$\mathbf{L}_{rr} = \mathbf{L}_r^T \mathbf{L}_r = \begin{bmatrix} \mathbf{I}_{3\times 3} & \mathbf{0}_{3\times 3} \\ \mathbf{0}_{3\times 3} & \mathbf{0}_{3\times 3} \end{bmatrix} \tag{38}$$

ACKNOWLEDGMENT

This paper summarizes the main activity carried out during A. Rizza PhD research under the supervision of Prof. Francesco Topputo. For the contribution proposed in this work the author would like to thanks Prof. Paolo Panicucci and PhD Candidate Carmine Buonagura for the help received in modeling the variable density gravity field as well as the PostDoc researcher Carmine Giordano for the continuous feedback received along the way.

REFERENCES

[1] D. J. Scheeres, *Orbital motion in strongly perturbed environments: applications to asteroid, comet and planetary satellite orbiters*. Springer Berlin, Heidelberg, 2016. Chapter 1-2, 10.1007/978-3-642-03256-1.

[2] D. Dunham, J. McAdams, and R. Farquhar, "NEAR mission design," *Johns Hopkins APL Technical Digest (Applied Physics Laboratory)*, Vol. 23, 01 2002.

[3] M. D. Rayman, "Lessons from the Dawn mission to Ceres and Vesta," *Acta Astronautica*, Vol. 176, 2020, pp. 233–237, 10.1016/j.actaastro.2020.06.023.

[4] K. M. Getzandanner, P. G. Antreasian, M. C. Moreau, J. M. Leonard, C. D. Adam, D. Wibben, K. Berry, D. Highsmith, and D. Lauretta, "Small body proximity operations & TAG: Navigation experiences & lessons learned from the OSIRIS-REx mission," *AIAA SciTech Forum*, p. 2387, 10.2514/6.2022-2387.

[5] M. Yoshikawa, J. Kawaguchi, A. Fujiwara, and A. Tsuchiyama, "Chapter 6 - The Hayabusa mission," *Sample Return Missions: The Last Frontier of Solar System Exploration. Editor: Andrea Longobardo. Elsevier* (A. Longobardo, ed.), pp. 123–147, 2021, 10.1016/B978-0-12-818330-4.00006-9.

[6] S. Watanabe, Y. Tsuda, M. Yoshikawa, S. Tanaka, T. Saiki, and S. Nakazawa, "Hayabusa2 mission overview," *Space Science Reviews*, Vol. 208, 2017, pp. 3–16, 10.1007/s11214-017-0377-1.

[7] A. Accomazzo, P. Ferri, S. Lodiot, J.-L. Pellon-Bailon, A. Hubault, R. Porta, J. Urbanek, R. Kay, M. Eiblmaier, and T. Francisco, "Rosetta following a living comet," *Acta Astronautica*, Vol. 126, 2016, pp. 190–198, 10.1016/j.actaastro.2016.04.023.

[8] A. F. Cheng, A. S. Rivkin, P. Michel, J. Atchison, O. Barnouin, L. Benner, N. L. Chabot, C. Ernst, E. G. Fahnestock, M. Kueppers, P. Pravec, E. Rainey, D. C. Richardson, A. M. Stickle, and C. Thomas, "AIDA DART asteroid deflection test: Planetary defense and science objectives," *Planetary and Space Science*, Vol. 157, 2018, pp. 104–115, https://doi.org/10.1016/j.pss.2018.02.015.

[9] E. S. Rainey, A. M. Stickle, A. F. Cheng, A. S. Rivkin, N. L. Chabot, O. S. Barnouin, C. M. Ernst, A. I. S. W. Group, *et al.*, "Impact modeling for the Double Asteroid Redirection Test (DART) mission," *International Journal of Impact Engineering*, Vol. 142, 2020, p. 103528, 10.1016/j.ijimpeng.2020.103528.

[10] R. Walker, D. Binns, C. Bramanti, M. Casasco, P. Concari, D. Izzo, D. Feili, P. Fernandez, J. G. Fernandez, P. Hager, *et al.*, "Deep-space CubeSats: thinking inside the box," *Astronomy & Geophysics*, Vol. 59, No. 5, 2018, pp. 5–24.

[11] F. De Novaes Kucinskis and M. G. V. Ferreira, "Taking the ECSS autonomy concepts one step further," *SpaceOps 2010 Conference "Delivering on the Dream" Hosted by NASA Mars*, 2010, pp. 25–30, 10.2514/6.2010-2364.

[12] D. A. Surovik, *Autonomous mission design in extreme orbit environments*. PhD thesis, University of Colorado at Boulder, 2016.

[13] F. Capolupo, T. Simeon, and J. C. Berges, "Heuristic guidance techniques for the exploration of small celestial bodies," *IFAC-PapersOnLine*, Vol. 50, No. 1, 2017, pp. 8279–8284, 10.1016/j.ifacol.2017.08.1401.

[14] A. Rizza, C. Giordano, and F. Topputo, "Goal-Oriented Guidance Strategy for Binary Asteroid Exploration: Investigation of Different Metrics," *45th AAS Guidance, Navigation and Control Conference*, Breckenridge, CO, 2023, pp. 1–14.

[15] A. Rizza, C. Giordano, and F. Topputo, "A goal-oriented guidance approach for binary asteroids exploration," *Astrodynamics*, 2024. In Press.

[16] A. Rizza, F. Topputo, and S. D'Amico, "Goal-oriented asteroid mapping under uncertainties using Sequential Convex Programming," *AIAA SciTech Forum*, 2024, 10.2514/6.2024-1990.

[17] X. Liu and P. Lu, "Solving nonconvex optimal control problems by convex optimization," *Journal of Guidance, Control, and Dynamics*, Vol. 37, No. 3, 2014, pp. 750–765, 10.2514/1.62110.

[18] Y. Mao, M. Szmuk, X. Xu, and B. Açikmese, "Successive convexification: A superlinearly convergent algorithm for non-convex optimal control problems," 2018, 10.48550/arXiv.1804.06539.

[19] R. A., *Goal-oriented guidance under uncertainties for small bodies exploration*. PhD thesis, Politecnico di Milano, 2024.

[20] D. A. Vallado, *Fundamentals of astrodynamics and applications*, Vol. 12. Springer Science & Business Media, 2001.

[21] S. Boyd and L. Vandenberghe, *Convex Optimization*. Cambridge University Press, 2004, 10.1017/CBO9780511804441.

[22] D. Malyuta, T. P. Reynolds, M. Szmuk, T. Lew, R. Bonalli, M. Pavone, and B. Açıkmeşe, "Convex Optimization for Trajectory Generation: A Tutorial on Generating Dynamically Feasible Trajectories Reliably and Efficiently," *IEEE Control Systems Magazine*, Vol. 42, No. 5, 2022, pp. 40–113, 10.1109/MCS.2022.3187542.

[23] Y. Mao, D. Dueri, M. Szmuk, and B. Açıkmeşe, "Successive convexification of non-convex optimal control problems with state constraints," *Ifac-PapersOnline*, Vol. 50, No. 1, 2017, pp. 4063–4069, 10.1109/CDC.2016.7798816.

[24] S. Laurens, M. Jouisse, and P. Seimandi, "State vector uncertainty and maneuver errors: analysis of the early orbit and station-keeping phases of an electrical satellite," *8th - Space Debris Conference, ESA*, ESA/ESOC Darmstadt, Germany, 2021.

[25] M. Grant and S. Boyd, "Graph implementations for nonsmooth convex programs," *Recent Advances in Learning and Control* (V. Blondel, S. Boyd, and H. Kimura, eds.), Lecture Notes in Control and Information Sciences, pp. 95–110, Springer-Verlag Limited, 2008. `http://stanford.edu/~boyd/graph_dcp.html`.

[26] I. Polik, T. Terlaky, and Y. Zinchenko, "SeDuMi: a package for conic optimization," *IMA workshop on Optimization and Control, Univ. Minnesota, Minneapolis*, Citeseer, 2007.

[27] A. Rizza, C. Bonagura, P. Panicucci, and F. Topputo, "Modular Pipeline for Small Bodies Gravity Field Modeling: Enhancing accuracy and efficiency for proximity operations," *75th International Astronautical Congress 2024 (IAC2024)*, 2024, 10.48550/arXiv.2409.02531.

[28] C. Froeschlé, E. Lega, and R. Gonczi, "Fast Lyapunov indicators. Application to asteroidal motion," *Celestial Mechanics and Dynamical Astronomy*, Vol. 67, No. 1, 1997, pp. 41–62, 10.1023/A:1008276418601.

[29] J. Daquin, R. Pédenon-Orlanducci, M. Agaoglou, G. García-Sánchez, and A. M. Mancho, "Global dynamics visualisation from Lagrangian Descriptors. Applications to discrete and continuous systems," *Physica D: Nonlinear Phenomena*, Vol. 442, 2022, p. 133520, 10.1016/j.physd.2022.133520.

[30] K. Oguri and J. W. McMahon, "Robust Spacecraft Guidance Around Small Bodies Under Uncertainty: Stochastic Optimal Control Approach," *Journal of Guidance, Control, and Dynamics*, Vol. 44, No. 7, 2021, pp. 1295–1313, 10.2514/1.G005426.

[31] N. Stacey and S. D'Amico, "Autonomous swarming for simultaneous navigation and asteroid characterization," *AAS/AIAA Astrodynamics Specialist Conference*, Vol. 1, 2018, p. 76.

[32] C. Giordano, "Characterization of Gauss–Markov stochastic sequences for mission analysis," *Astrodynamics*, Vol. 8, No. 1, 2024, pp. 135–148, 10.1007/s42064-023-0183-3.

[33] D. Kuettel, *Autonomous Guidance Around Small Bodies Using Continuous-Thrust Propulsion*. PhD thesis, University of Colorado Boulder, 2021.